NeuroImage **18,** 143–155 (2003)
doi:10.1006/nimg.2002.1299

An Algorithm for Rapid Calculation of a Probabilistic Functional Atlas of Subcortical Structures from Electrophysiological Data Collected during Functional Neurosurgery Procedures

Wieslaw L. Nowinski,* Dmitry Belov,* and Alim-Louis Benabid†

**Institute of Bioengineering, 21 Heng Mui Keng Terrace, 119613 Singapore; and*
†Joseph Fourier University School of Medicine, Grenoble, France

Received January 24, 2002

The paper introduces an optimal algorithm for rapid calculation of a probabilistic functional atlas (PFA) of subcortical structures from data collected during functional neurosurgery procedures. The PFA is calculated based on combined intraoperative electrophysiology, pre- and intraoperative neuroimaging, and postoperative neurological verification. The algorithm converts the coordinates of the neurologically most effective contacts into probabilistic functional maps taking into account the geometry of a stimulating electrode. The PFA calculation comprises the reconstruction of the contact coordinates from two orthogonal projections, normalizing (warping) the contacts modeled as cylinders, voxelizing the contact models, calculating the atlas, and computing probability. In addition, an analytical representation of the PFA is formulated based on Gaussian modeling. The initial PFA has been calculated from the data collected during the treatment of 274 Parkinson's disease patients, most of them operated bilaterally (487 operated hemispheres). It contains the most popular stereotactic targets, the subthalamic nucleus, globus pallidus internus, and ventral intermedius nucleus. The key application of the algorithm is targeting in stereotactic and functional neurosurgery, and it also can be employed in human and animal brain research. © 2002 Elsevier Science (USA)

Key Words: **probabilistic functional atlas; electronic brain atlases; stereotactic and functional neurosurgery; brain mapping; electrophysiology; voxelization; Gaussian modeling.**

INTRODUCTION

A number of stereotactic printed brain atlases have been constructed since the 1950s [1, 3, 34, 35, 38–40, 46]. To combine the widely accepted and used printed atlases with the capabilities offered by electronic atlases, several printed atlases have been converted into electronic form, including the Schaltenbrand–Bailey atlas [14, 16, 48], the Schaltenbrand–Wahren atlas [14, 15, 23, 27, 37], the Talairach–Tournoux atlas [14, 26], the referentially oriented Talairach–Tournoux atlas [26], the Ono *et al.* atlas [27], the Afshar *et al.* atlas [22], and the Van Buren–Borke atlas [14].

There are two major limitations in using the current electronic brain atlases for stereotactic and functional neurosurgery. First, these atlases are constructed from only a few brains. Second, they are anatomical, while the actual stereotactic targets are functional. This paper addresses the construction of a probabilistic functional atlas that overcomes both limitations and opens new possibilities, particularly in providing community-centric solutions in stereotactic and functional neurosurgery [25] and potentially in human and animal brain research.

During surgical procedures, such as the treatment of Parkinson's disease, microelectrodes or macroelectrodes are inserted into the patient's brain to map it to identify stereotactic targets. This mapping locates the functional positions of structures in the brain, as each structure has its own characteristic firing pattern. After localizing the target by microelectrode recording, the microelectrode is replaced by a permanent, stimulating electrode containing one or more contacts. By knowing the coordinates of the contacts and their size and electrophysiological properties, the activated region within the studied structure can be determined. Several electrodes may be inserted into the patient's brain during surgery, either unilaterally or bilaterally, providing information about the functional location of cerebral structures. By collecting data from numerous patients, it is possible to construct probabilistic maps showing functional distribution of subcortical structures. These functional probabilistic maps have a great importance in treatment, particularly in surgery of movement disorders, and in human and animal brain research.

The goal of this paper was to formulate an algorithm for rapid calculation of a probabilistic functional atlas from electrophysiological and neuroimaging data and to present the initially calculated atlas.

1053-8119/02 $35.00

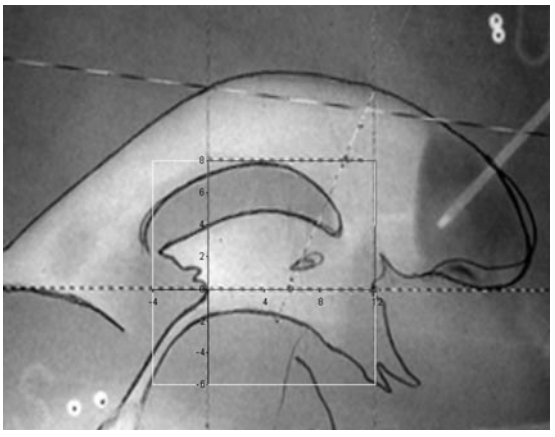

FIG. 1. X ray showing the anterior and posterior commissures and the thalamus. The coordinates of the electrode and the landmarks are measured on two different pairs of orthogonal projections.

MATERIAL AND METHOD

We define the following. An *electrode* is a probe inserted into the brain employed for recording or stimulation. A stimulating electrode has one or more cylindrical contacts. A *contact* is modeled as a cylinder; however, generally the method proposed here does not limit the model of contact, and it may be of any arbitrary shape. The *best contact* of a multicontact electrode is the contact which is clinically most active during postoperative neurological assessment of the patient. The *best electrode* is that electrode which contains the best contact(s). The results are calculated and presented in the *atlas space,* which is a three-dimensional (3D) Cartesian space. Any point or vector with coordinates x, y, and z in this space is denoted by (x, y, z). A *structure* is a part of the brain for which its functional distribution is calculated in the atlas space. The *probabilistic functional atlas* (PFA) or *atlas* is a function that characterizes the spatial frequency of the best contacts. The atlas value in point (x, y, z) is denoted by $a(x, y, z)$. The *best atlas target* is this subset of a given structure where the atlas has the maximum value.

2.1. Material

High accuracy electrophysiological and neuroimaging data have been collected for several years by the third author and are available for hundreds of patients, most of them operated bilaterally. For this study, we used 274 patients, 487 hemispheres, and 500 best contacts.

The operating room environment for data collection has been described [4]. A neurosurgical robot, NeuroMate (Integrated Surgical Systems, France), was used for positioning the electrodes and their locations we imaged intraoperatively by two X rays. For data acquisition, the Ben-gun (Integrated Surgical Systems, France) was employed in most cases. The data for this study comprise the positions of the chronically implanted electrodes and their best (clinically most active) contacts. An electrode contains one or four cylindrical contacts. For each patient, the locations of the anterior and posterior commissures, the height of the thalamus, and the width of the third ventricle were measured preoperatively on two orthogonal X-ray ventriculography images followed by the measurement of the positioning of the electrode(s) on an intraoperative pair of X rays (Fig. 1). The use of X ray gave undistorted data which subsequently were measured with high accuracy, 0.2–0.3 mm. It should be noted that MRI was not used to get the coordinates because it may result in geometric distortions of a few millimeters, while the surgical procedure requires submillimeter accuracy.

The electrophysiological and imaging data collected for each patient are given in the data space. This space uses the millimeter as unit. To build the probabilistic functional atlas, these data have to be normalized and placed in the atlas space. The atlas space is based on the same four landmarks identified in the patient's data: posterior commissure (PC), anterior commissure (AC), height of the thalamus (HT), and width of the third ventricle (V_3) (Fig. 1). The atlas space was constructed on the following reference axes (Fig. 2): The x axis anteroposteriorly passing through the PC and AC. This axis is scaled in PC–AC units and the distance between the PC and AC is 12 PC–AC units. The y axis laterally passing through the PC. This axis is scaled in millimeters. The z axis dorsoventrally passing through the PC. This axis is scaled in HT units and the height of the thalamus has 8 HT units.

The (continuous) atlas space was sampled uniformly with the user-defined step resulting in cubic voxels. To transform the original patient data given in millimeters to the atlas space units, their approximate average values were taken, HT = 16 mm, ACPC = 24 mm, and V_3 = 6 mm.

2.2. Method

2.2.1. General Description of the Algorithm

The flow chart of the algorithm for the construction of the probabilistic functional atlas is shown in Fig. 3. The atlas was constructed from the best contacts. The positions of these contacts were reconstructed from two orthogonal X rays and placed in the atlas space by applying spatial normalization. The normalized (warped) contacts were voxelized, the atlas function was calculated, and finally the probability was computed.

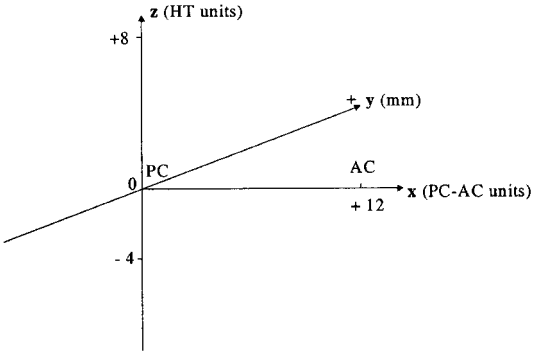

FIG. 2. Probabilistic functional atlas coordinate system.

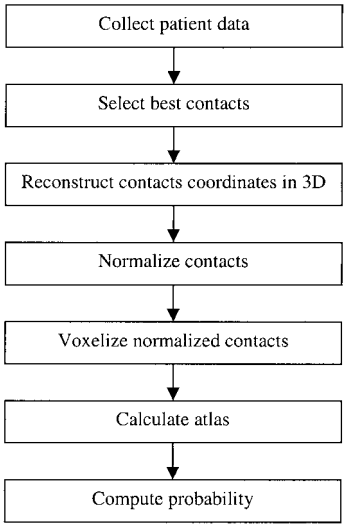

FIG. 3. Flowchart of the algorithm for calculation of the probabilistic functional atlas.

2.2.2. Patient Data Collection

The collected patient data were kept, processed, and presented as a four-level tree structure. The first level is the list of subcortical structures. At the second level, for each structure the list of patients (or subjects) is given. At the third level, for each patient the list of electrodes is provided along with their type and status (best, not best). The type of electrode uniquely identifies its geometry, including diameter, number of contacts, contact height, and gap between contacts. At the fourth level, for each electrode the list of its contacts is given. Each contact has its identifier, coordinates, and status (best, not best). Either the complete data tree or any subtree containing the data of interest can be selected for the calculation of the probabilistic functional atlas.

2.2.3. Best Contact Selection

In the majority of cases, deep brain stimulating electrodes with four contacts were employed. The initial best contacts were determined during the surgery. Subsequently, the best contacts were verified postoperatively in a neurological assessment. As the contacts are switchable, the most neurologically effective contact was selected. In a few cases, two best contacts were selected for a single electrode (hence their number is 500, while the number of the best electrodes is only 487).

2.2.4. Contact Coordinate Reconstruction in 3D

The 3D coordinates of the contact are easily reconstructed from two orthogonal X-ray projections. For this purpose, we determined the physical coordinate system with center O, positions of two X-ray sources and image plates in this coordinate system, and both projections of O to orthogonal X-ray images resulting in O_1 and O_2. By measuring on the X-ray images the position of a contact against O_1 and O_2, we obtained input data for a trivial geometrical problem of reconstructing, a 3D point from its two orthogonal projections given the positions of the X-ray sources.

2.2.5. Contact Normalization

The surgical procedure has been performed successfully for several years by the third author. Continuous enhancement and vast experience result in excellent outcomes and high accuracy of the data collected. This procedure was based on the available robust landmarks determined from X rays, i.e., AC, PC, HT, and V_3. The spatial normalization used in our algorithm followed surgery planning. The coordinates of the best contact(s) were scaled anteroposteriorly proportionally to the intercommissural distance AC–PC, dorsoventrally proportionally to the height of thalamus HT, and compensated laterally against the third ventricle, V_3.

Let (x', y', z'), (x, y, z) be a point in the data space and atlas space, respectively. Moreover, for a given brain specimen in the data space, let us denote l as AC–PC length, g as the height of the thalamus, and v as the width of third ventricle. The transformation from the atlas space to the data space is

$$x' = \frac{x \times l}{\mathrm{ACPC}}, y' = y \otimes \left(\frac{V_3}{2} - \frac{v}{2}\right), z' = \frac{z \times g}{\mathrm{HT}}. \quad (1)$$

The transformation from the data space to the atlas space is done as follows

$$x = \frac{x' \times \mathrm{ACPC}}{l}, y = y' \otimes \left(\frac{v}{2} - \frac{V_3}{2}\right), z = \frac{z' \times \mathrm{HT}}{g}, \quad (2)$$

where sign $\otimes$ depends on the location of electrode; if it is in the left hemisphere then the sign is "+"; otherwise it is "−."

2.2.6. Normalized Contact Voxelization and Atlas Calculation

Contact voxelization and atlas calculation can be done efficiently within one procedure having two loops, so we describe these two steps jointly. The principle of atlas construction is illustrated in Fig. 4 and the corresponding flowchart of the algorithm is diagrammed in Fig. 5.

The atlas function $a(x, y, z)$ was set initially to zero. Then, all best contacts were processed such that for each best contact and for every voxel with a center (x, y, z) inside this contact, the atlas function in this voxel was increased by 1, i.e., $a(x, y, z) := a(x, y, z) + 1$. After processing all best contacts, function $a(x, y, z)$ contains the value of the atlas for a given structure.

The key problem in voxelization is finding all voxels that intersect a considered cylinder. This particular problem is part of a general class of problems in computer science aiming at a discrete representation of continuous (real) objects. There are a vast number of problems in this field ranging from the representation of the real numbers as floating point numbers to discrete representation of objects, such as a hypersphere [2]. Several voxelization approaches have been proposed [e.g., [2, 6, 36], but none of them addresses an efficient voxelization of a cylinder. Another problem is alias-

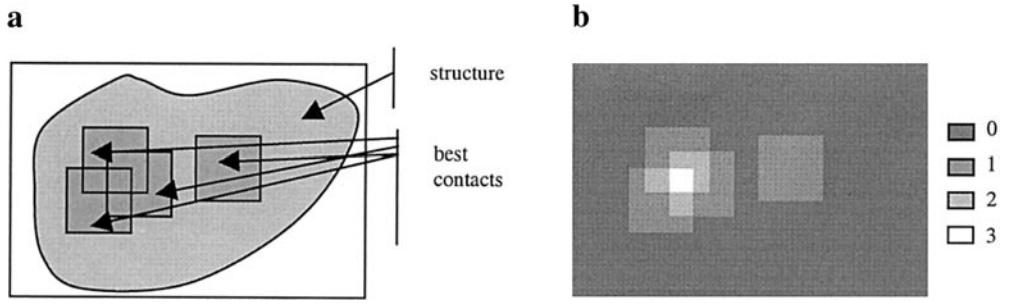

FIG. 4. The principle of calculation of the atlas in a two-dimensional case: (a) arrangement of the best contacts within the structure and (b) the resulting probabilistic map.

ing and the recent methods for alias-free voxelization have been presented [36].

Our algorithm voxelizes not just a circular truncated cylinder but also a transformed cylinder which can be an elliptical cylinder or cylinder warped nonlinearly along the *z* axis. For this purpose we introduce a new concept.

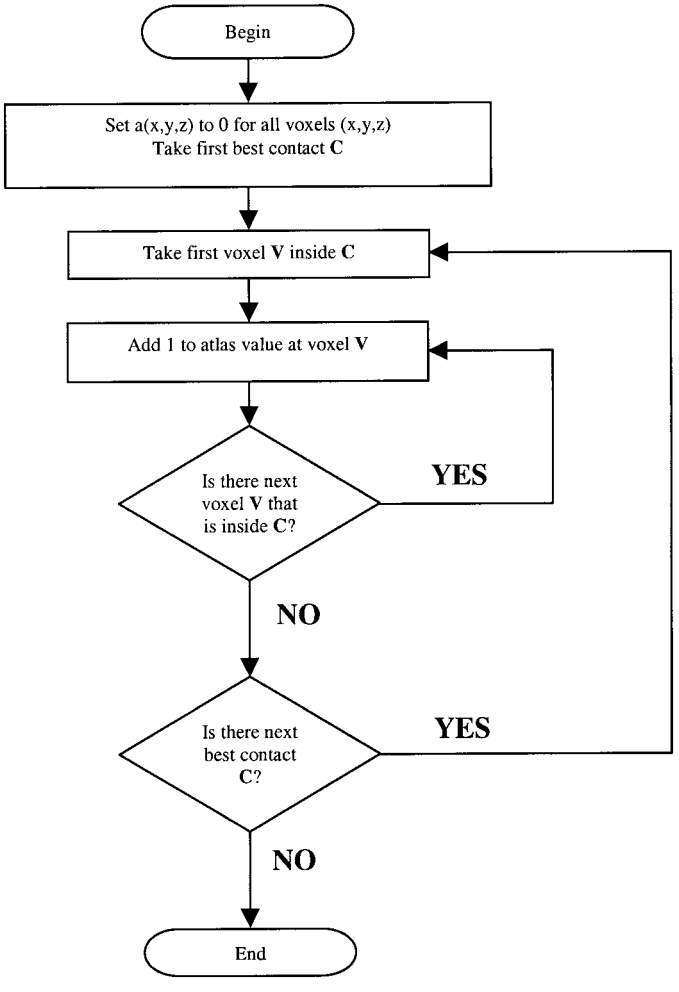

FIG. 5. Flowchart of the algorithm for calculation of the atlas function.

Definition NL. Homeomorphism T is NL transformation if and only if T is a linear combination of a linear scaling along the x and y axes, linear or nonlinear (one-to-one, continuous) scaling along the z axis, and linear translation along the x, y, z axes.

Rotation can also be applied before T, as it does not change the form of cylinder. Thus, NL transformation is more general than an affine transformation as a nonlinear scaling along the z axis is allowed. We denote by T^{-1} the inverse transformation of T. Obviously T^{-1} is also NL transformation.

Mathematically, a problem of locating a point relative to a cylinder is simple. Computationally, this problem is more demanding, as all best cylindrical contacts and all voxels in the atlas space relative to a selected cylindrical contact have to be processed. At the same time, the atlas calculation must be fast to allow its interactive calculation, particularly in remote operations.

We define (Fig. 6) r as the radius of a cylinder, h as the height of a cylinder, $a = (x_1, y_1, z_1)$ as the inferior tip of a cylinder (by "tip" we mean one extreme of the longitudinal axis of cylinder), $b = (x_2, y_2, z_2)$ as the superior tip of a cylinder (without loss of generality we assume that $z2$ is greater than or equal to $z1$), and T as the transformation satisfying Definition NL. For PFA generation, we chose T and T^{-1} based on the spatial normalization given in section 2.2.5.

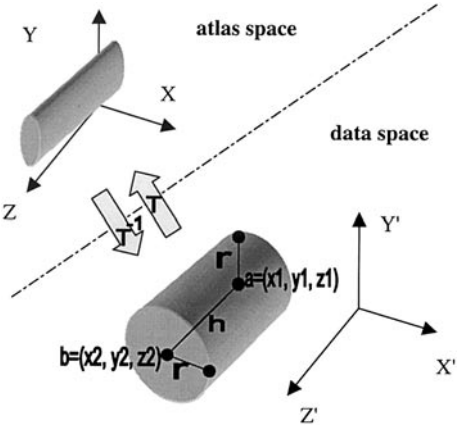

FIG. 6. Illustration of the definitions in the cylindrical contact.

The general idea of cylinder voxelization is to find the limits of its two coordinates (x, y) (Appendix 1). Then, by fixing these coordinates within their limits, the limit of the third coordinate z is found (Appendix 2). In this way, all points (x, y, z) within the cylinder can be obtained.

Voxelization algorithm. The atlas space is subdivided by voxels, each with a size of $h_x \times h_y \times h_z$. The voxelization algorithm performs the following steps applied to each best cylindrical contact: 1. Find the minimum and maximum limits of x and y for the cylinder and denote them by $x'_{\min}$, $x'_{\max}$ and $y'_{\min}$, $y'_{\max}$, respectively (as described in Appendix 1). 2. By using transformation T, transform $x'_{\min}$, $x'_{\max}$ and $y'_{\min}$, $y'_{\max}$ to the atlas space. The results are $x_{\min}$, $x_{\max}$ and $y_{\min}$, $y_{\max}$, respectively. 3. By using transformation T^{-1}, transform h_x and h_y to the data space. The resulting values are h'_x and h'_y. As a result, for any point (x, y) from rectangle $[x_{\min}, x_{\max}] \times [y_{\min}, y_{\max}]$, there is a unique corresponding point (x', y') from rectangle $[x'_{\min}, x'_{\max}] \times [y'_{\min}, y'_{\max}]$ and vice versa. 4. Let $x'(x)$ be in range $[x'_{\min}, x'_{\max}]$ ($[x_{\min}, x_{\max}]$) with step $h'_x(h_x)$, $y'(y)$ be in range $[y'_{\min}, y'_{\max}]$ ($[y_{\min}, y_{\max}]$) with step $h'_y(h_y)$. For every point (x', y') ((x, y)), the following operations are performed: 4.1. If there is a range of z coordinate $[z'_{\min}, z'_{\max}]$ such that segment $e'f'$ belongs to the cylinder, where $e' = (x', y', z'_{\min})$ and $f' = (x', y', z'_{\max})$ (as described in Appendix 2), then the following steps are performed: 4.1.1. By using transformation T, transform $z'_{\min}$ and $z'_{\max}$ to the atlas space and denote them by $z_{\min}$ and $z_{\max}$, respectively. 4.1.2. For each voxel (x_c, y_c, z_c) containing point (x, y, z), where z is changing from $z_{\min}$ to $z_{\max}$ with step h_z, $a(x_c, y_c, z_c) := a(x_c, y_c, z_c) + 1$.

As this algorithm finds all voxels which are intersected by a cylinder, one can easily modify it to select, for instance, voxels with centers inside or on the cylinder. An example of a voxelized contact modeled as a cylinder is shown in Fig. 7.

Once the atlas has been constructed, the surfaces of its structures can optionally be smoothed using antialiasing [11]. Antialiasing can also be done on the fly as follows. Let S be the volume of a voxel and S' the volume of that part of the voxel which belongs to the best contact. Then atlas value inside the voxel is increased by the ratio of S' by S.

The total complexity of the algorithm is bounded by $O(N \times M)$, where N is the number of best contacts and M is the maximum number of voxels that can be intersected by one contact. This means that the voxelization algorithm is optimal in space and complexity. Indeed, we consider voxels as elements of the atlas only in step 4.1.2, but from Appendixes 1 and 2 it follows that all those voxels are inside the cylinder or they intersect it. An additional advantage is that for each (x, y) we find the whole column of voxels intersected by the cylinder, which substantially speeds up the PFA generation.

FIG. 7. The contact modeled as cylinder placed in a discrete (voxelized) space.

2.2.7. Probability Computation

To compute atlas probability, the atlas function has to be suitably scaled. We propose two scaling approaches: (1) intuitive, easy to understand and use by clinicians, and (2) formal, defined in a mathematical sense.

Let V denote the integral of $a(x, y, z)$ over the whole space, N be the total number of best contacts, MAX denote the maximum value of atlas $a(x, y, z)$, and CONST denote a constant value that corresponds to some assumed MAX. Probability $p(x, y, z)$ of a given structure at point (x, y, z) can be calculated in one of the following ways: 1. $p(x, y, z) = a(x, y, z)/N$. 2. $p(x, y, z) = a(x, y, z)/\text{MAX}$. 3. $p(x, y, z) = a(x, y, z)/\text{CONST}$. 4. $p(x, y, z) = a(x, y, z)/V$.

Probability definition 1 gives the fraction of the best contacts within the structure to the total number of contacts used to study this structure. Probability definition 2 indicates the fraction of the best contacts to the maximum spatial frequency of the contacts. Probability definition 3 tells what is the fraction of the best contacts to some assumed maximal density, which the user can set to determine the level of confidence to his data. These definitions do not fulfill the mathematical definition of probability; however, they are useful practically. Probability definition 4 is in a mathematical sense; however, its clinical meaning is not obvious.

The best target is calculated as the region where the probability of a given structure is maximum.

2.3. Analytical Representation

The above algorithm calculates a useful distribution of a studied structure provided that the number of best contacts employed is sufficiently high. For instance, assuming a uniform distribution of the best contacts within a structure, their number should be bigger than the ratio of the volume of the structure to the volume of the contact. When the number of the available best contacts is not sufficient, the originally calculated atlas is not smooth in terms of shape and value, and it may not be determined (remain zero) in some regions (Fig. 8). In this case, the values of the atlas can be treated as samples with Gaussian distribution from which a smooth, analytical atlas is reconstructed.

Denoting

$$V = \int_{-\infty}^{+\infty} \int_{-\infty}^{+\infty} \int_{-\infty}^{+\infty} a(x, y, z)\,dx\,dy\,dz,$$

we introduce the joint probability density of a random vector

$$w = \begin{pmatrix} x \\ y \\ z \end{pmatrix}$$

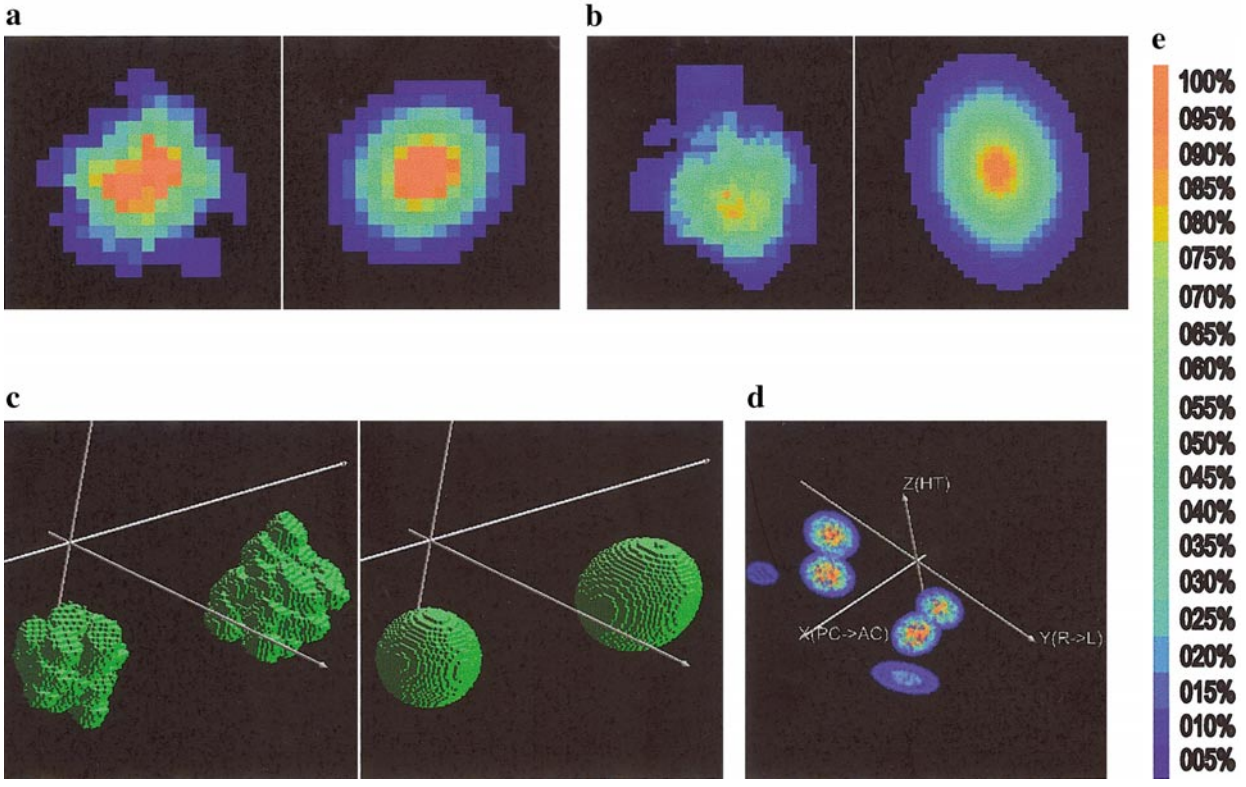

FIG. 8. Probabilistic functional atlas: (a) (left) STN sagittal slice calculated with 0.5-mm resolution from 303 contacts; (right) corresponding analytical slice; (b) (left) VIM coronal slice calculated with 0.25-mm resolution from 111 contacts; (right) corresponding analytical slice; (c) (left) 3D STN calculated with 0.25-mm resolution from 303 contacts; (right) corresponding analytical structure; (d) 3D STN, VIM, and GPI structures calculated with 0.5-mm resolution presented as semitransparent objects with the opacity proportional to the probability; (e) probability color palette.

by

$$p(x, y, z) = \frac{a(x, y, z)}{V}. \tag{3}$$

Without loss of generality, let us consider x coordinate. Then

$$\mu_x = \int_{-\infty}^{+\infty} x p(x) dx$$

is the mean value of x,

$$\sigma_x = \sqrt{\int_{-\infty}^{+\infty} (\chi - \mu_x)^2 p(x) dx}$$

is the standard deviation of x, and

$$p(x) = \int_{-\infty}^{+\infty} \int_{-\infty}^{+\infty} p(x, y, z) dy dz$$

is the marginal probability density of x. Thus, we create a trivariate Gaussian with the joint probability density

$$g(x, y, z) = g(w) = \frac{1}{\sqrt{(2\pi)^3 |M|}} e^{-1/2 (w - \mu)^T M^{-1} (w - \mu)}, \tag{4}$$

where

$$\mu = \begin{pmatrix} \mu_x \\ \mu_y \\ \mu_z \end{pmatrix} \text{ and } M = \begin{pmatrix} \sigma_x^2 & m_{xy} & m_{xz} \\ m_{xy} & \sigma_y^2 & m_{yz} \\ m_{xz} & m_{yz} & \sigma_z^2 \end{pmatrix}$$

is a nonsingular second moment matrix. By using Eqs. 3 and 4, we determine the analytical atlas function as

$$a(x, y, z) = V g(x, y, z). \tag{5}$$

From the properties of the normal distribution it follows that a structure is represented geometrically as a three-dimensional ellipsoid with center in μ and semiaxis vectors

TABLE 1

Performance of the PFA Calculation

	Atlas resolution (seconds)	
	0.5 mm	0.25 mm
PFA calculation from 10000 simulated best contacts	1.352	5.498
PFA calculation from 20000 simulated best contacts	2.614	10.906
Analytical representation	1.192	6.379

$$\left(3\sigma_x \frac{v_x}{|v_x|},\ 3\sigma_y \frac{v_y}{|v_y|},\ 3\sigma_z \frac{v_z}{|v_z|}\right),$$

where

$$M^{-1} = \begin{pmatrix} v_x^T \\ v_y^T \\ v_z^T \end{pmatrix} \begin{pmatrix} \lambda_x & 0 & 0 \\ 0 & \lambda_y & 0 \\ 0 & 0 & \lambda_z \end{pmatrix} (v_x,\ v_y,\ v_z), \begin{pmatrix} \lambda_x \\ \lambda_y \\ \lambda_z \end{pmatrix}$$

are eigenvalues of M^{-1}, and (v_x, v_y, v_z) are eigenvectors of M^{-1} (Fig. 8).

Having calculated $g(x, y, z)$, we have to check how adequate the created Gaussian model $g(x, y, z)$ is to the original probability $p(x, y, z)$. For this purpose, one can use the Pearson χ^2 test [18] or the Kolmogorov–Smirnov test [18]. If $g(x, y, z)$ does not satisfy any of these tests, multiple Gaussian modeling can be attempted. By clustering the atlas voxels [33], a Gaussian model can be formulated for each cluster.

3. RESULTS AND DISCUSSION

An efficient algorithm for the calculation of the PFA has been developed and validated. The PFA has been constructed from the electrophysiological and neuroimaging data collected for the most popular stereotactic targets, including the subthalamic nucleus (STN), globus pallidus internus (GPI), and ventral intermedius nucleus (VIM). Figure 8 shows some 2D (slices) and 3D (volumetric models) examples of the calculated and analytically represented atlas structures.

The complexity of this algorithm is proportional to the number of best contacts and the number of voxels (i.e., it depends on atlas resolution, which can be set by the user interactively). The complexity of (single) Gaussian modeling is proportional to the number of voxels and does not depend on the number of best contacts. The performance of calculation of the PFA is summarized in Table 1. With the current population of 500 best contacts, the atlas is calculated in near real-time.

The construction of probabilistic atlases is an active area of research [17, 20, 21, 43, 45]. Probabilistic atlases store information on anatomical and functional variability in a population, such as how the brain varies in health [5, 31] and disease [42] as well as across gender, age, and time. Figure 9 illustrates our attempt to classify these efforts. The anatomical probabilistic atlases may store information on the variability of a sulcus or gyrus [5, 17, 31] or be surface-based [47] or volumetric [8]. This subdivision corresponds roughly to variations in one-, two-, and three-dimensional manifolds. The differences between them, however, may not be distinctive enough. For instance, a sulcus may be modeled as a ribbon (2D surface) [17] or dynamic changes in the brain can be stored as 4D maps.

Existing tools, such as *BrainMap* [12] or *Brain Atlas for Functional Imaging* [29], facilitate metanalysis allowing for construction of probabilistic functional atlases from radiologic images. The resolution of fMRI or PET images, however, is low (several millimeters) and the size of activation regions may be quite large. On the other hand, a microelectrode is able to measure the signal from a single neuron. In our approach, the accuracy of the collected data is 0.2–0.3 mm, while the resolution of the calculated atlas is user-dependent. As the calculation of an atlas is fast (Table 1), the user can recalculate it easily. Practically, we compute and manipulate the atlas with 0.25-mm (for a single structure) or 0.5-mm (for multiple structures) resolutions on a standard personal computer.

To the best of our knowledge, the PFA created by us is the first volumetric probabilistic functional atlas developed. A related effort is the development of an electrophysiological database of deep brain functional anatomy [10]. It exploits a coding structure [41] facilitated through the use of a novel graphical interface. The database stores points with related information mapped along stereotactic trajectories. From a surgical perspective, this approach has several limitations. It does not take into account the geometry of electrodes. The postoperative data are not available (the surgical procedure involves permanent therapeutic lesioning as opposed to the deep brain stimulation employed in our approach). The use of preoperative MRI only may result in geometric distortions

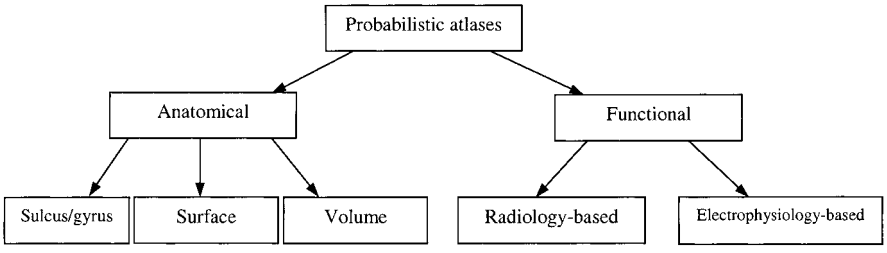

FIG. 9. Taxonomy of probabilistic atlases.

(potentially to several millimeters), while we additionally employ X rays resulting in 0.2–0.3 mm accuracy. On the other hand, the availability of volumetric data such as MRI allows for applying nonlinear warping, which is critical when dealing with cortical structures (but, as referenced below, practically negligible for subcortical structures) and the approach [10] exploits the ANIMAL algorithm for this purpose. Unfortunately, this algorithm does not take into account the locations of the AC and PC, which results in a substantial error for the deep brain structures. The error due to inaccurate location of the AC and PC is up to 5 mm [24] and the lack of identification of the intercommissural landmarks may result even in a higher error.

The resulting PFA depends on contact spatial normalization; however, voxelization of contacts is normalization-independent provided that the warping function satisfies Definition NL. Alternatively, one can use a region growing-type voxelization to find all voxels which intersect a cylinder starting from a "seed" voxel inside the cylinder. This approach supports any warping homeomorphism but it is not optimal, as all necessary voxels and unnecessary ones, but neighboring them, have to be checked against Conditions 1 and 2 (Appendix 2).

The atlas calculation is a linear operation, so merging PFAs or updating a PFA with the new data is fast and efficient. This opens avenues in building applications providing neurosurgical community services [25].

Calculation of the PFA is very fast. The current data, collected for several years by the third author, can be processed remotely (by our public domain application, see below) in a few seconds. Any update of the PFA can be done remotely in near real-time. This makes the algorithm useful for web-based applications.

A detailed validation of the algorithm using the Monte Carlo method (which is beyond the scope of this paper) exists (Belov, D., and Nowinski, W. L. Optimal voxelization of a deformed cylinder, submitted for publication). In addition, we have developed a portal for planning stereotactic and functional neurosurgery procedures based on this algorithm (available for public use from *www.cerefy.com*) described in [49].

The proposed method has several limitations in terms of data acquisition, related neurosurgical procedures, designed algorithm, and application scope. Data acquisition is invasive and the method is not applicable to healthy (normal) individuals. The method, however, can also be applied to study animals. Another data acquisition-related limitation is the use of X-ray ventriculography to determine the accurate locations of the landmarks. Ventriculography is invasive and it is less preferred than preoperative MRI or CT imaging. For instance, a survey in [9] shows that MRI alone was used in 50% of the studied centers while ventriculography in combination with MRI in only 18%. The method is able to handle the landmarks obtained from imaging modalities other than ventriculography; however, the generated functional maps will not be so accurate (as the 0.25-mm achieved here) because of the limited image resolution and geometric distortions. The data used to calculate the probabilistic functional atlas have been acquired only for Parkinson's disease patients. A similar surgical procedure is performed in psychosurgery and for treatment of several other disorders, including epilepsy, pain, and movement disorders such as dystonia or tremor (there are about 300 of them). Hence, the data collected during these procedures can also be used to calculate the probabilistic functional maps of subcortical structures. On the other hand, the algorithm is not applicable to many other brain disorders, such as Alzheimer's disease, attention deficit–hyperactivity disorder, Huntington's disease, or schizophrenia.

The currently generated probabilistic functional maps are limited to the most popular stereotactic target structures, i.e., STN, GPI, and VIM. However, the algorithm is quite general and it is able to calculate functional maps for other subcortical structures provided the data are available.

The algorithm is limited to electrodes with cylindrical contacts, which practically is not a real shortcoming as the currently employed electrodes have cylindrical contacts (monopolar and quadripolar DBS 3387, 3389, Medtronic, Minneapolis). A more serious limitation is that the algorithm models the activation region to correspond to the shape of the contact, which is a simplification. A more advanced model requires knowledge of the electrophysiological properties of brain tissues and electrical properties of electrodes. The spatial normalization of contacts' positions is linear. Theoretically, nonlinear warping would be superior [44]. Practically, within the region between the AC and PC, where the stereotactic targets are located, the difference between the linear and nonlinear warping is negligible [7]. We think that a suitable definition of landmarks [28] and their accurate positioning [24] are rather more important for an overall accuracy.

The choice of landmarks is another area of potential improvement. Ventral scaling of STN based on the height of the thalamus is questionable. STN, when scaled anteroposteriorly, may be correlated more to other than the AC or PC landmarks in a region around the floor of the third ventricle. Lateral compensation against the width of the third ventricle is typically applied for GPI and VIM, but in case of STN this compensation increases its standard deviation (which is not desirable from a spatial normalization point of view). A structure-dependent normalization might be better; however, this would not facilitate building a probabilistic functional atlas consistent across all subcortical structures.

The generated maps allow calculating the volume of functional structure and studying the spectrum of its probabilities for the operated groups of patients but not for normals. Therefore, effects of neurodegenerative disorders of brain volume and function cannot be studied for humans. However, the algorithm, when applied to animal data, will be able to facilitate addressing these problems.

In summary, the features of our method include the following: the algorithm is optimal, efficient, and fast; an analytical model is developed which gives flexibility in discretization; a smooth (analytical) atlas can be optionally generated if the number of best contacts is not sufficient; different atlases can easily be merged, which facilitates fast updates; the user is able to interactively control the resolution of the generated atlas; the algorithm is suitable for remote operations, as the

atlas calculation is fast; and the method is limited to subcortical structures and functional neurosurgery procedures employing electrodes with cylindrical contacts.

The PFA overcomes the limitations of the current electronic brain atlases available in most of image-guided neurosurgery systems [25] and it will potentially replace them in the future. The method also serves as a framework for building the probabilistic functional atlas of all subcortical structures from combined electrophysiological and neuroimaging data. Finally, an analysis of the probabilistic functional maps generated by using the proposed algorithm constitutes a general method for studying functional properties of subcortical structures.

APPENDIX 1

Finding the Minimum and Maximum of Three Coordinates of a Cylinder

It is obvious that the minimum and maximum of the three coordinates of a cylinder are on its top and bottom layers (Fig. 10). A given point c (Fig. 10) is on the top layer of the cylinder because: (1) the angle between vectors ab and bc is right, (2) the length of vector bc is less than or equal to the radius of the cylinder r.

Let us consider the bottom layer first to find the minimum and maximum values for the three coordinates. Then, we have

$$\begin{cases} (x - x_1)(x_2 - x_1) + (y - y_1)(y_2 - y_1) + (z - z_1)(z_2 - z_1) = 0 \\ (x - x_1)^2 + (y - y_1)^2 + (z - z_1)^2 - r^2 \le 0 \end{cases}. \tag{6}$$

Let us find the minimum and maximum of x. As the aim function x and the functions in Eq. 6 are convex and differentiable, the following optimization problem is a problem of convex programming [13]

$$x \to \text{extremum}$$

$$\begin{cases} (x - x_1)(x_2 - x_1) + (y - y_1)(y_2 - y_1) + (z - z_1)(z_2 - z_1) = 0 \\ (x - x_1)^2 + (y - y_1)^2 + (z - z_1)^2 - r^2 \le 0 \end{cases}. \tag{7}$$

The corresponding Lagrange function is

$$f = x + \lambda_1((x - x_1)(x_2 - x_1) + (y - y_1)(y_2 - y_1) + (z - z_1)(z_2 - z_1)) + \lambda_2((x - x_1)^2 + (y - y_1)^2 + (z - z_1)^2 - r^2).$$

Let us find the stationary points of f which, if they exist, are the solutions of the problem. For this purpose, we solve

$$\begin{cases} \dfrac{\partial f}{\partial x} = 0 \\ \dfrac{\partial f}{\partial y} = 0 \\ \dfrac{\partial f}{\partial z} = 0 \\ \dfrac{\partial f}{\partial \lambda_1} = 0 \\ \dfrac{\partial f}{\partial \lambda_2} = 0 \end{cases}. \tag{8}$$

By solving Eq. 8 we get

$$x = x_1 \pm r\sqrt{\frac{(y_2 - y_1)^2 + (z_2 - z_1)^2}{(x_2 - x_1)^2 + (y_2 - y_1)^2 + (z_2 - z_1)^2}}. \tag{9}$$

The same approach is applied to find the minimum and maximum of y and z. Let

$$\alpha = \frac{x_2 - x_1}{h},\ \beta = \frac{y_2 - y_1}{h},\ \gamma = \frac{z_2 - z_1}{h}.$$

Then considering also the top layer, we can derive the extreme value in the top x_t, y_t, z_t and bottom layer x_b, y_b, z_b as

$$x_t = x_2 \pm r\sqrt{(\beta^2 + \gamma^2)},\ y_t = y_2 \pm r\sqrt{(\alpha^2 + \gamma^2)},\ z_t = z_2 \pm r\sqrt{(\alpha^2 + \beta^2)}$$

$$x_b = x_1 \pm r\sqrt{(\beta^2 + \gamma^2)},\ y_b = y_1 \pm r\sqrt{(\alpha^2 + \gamma^2)},\ z_b = z_1 \pm r\sqrt{(\alpha^2 + \beta^2)}. \tag{10}$$

Thus, the minimum and maximum values of the three coordinates can be obtained from Eq. 10. Finally, we get (1) minimum values, $n_x = \min(x_b, x_t)$, $n_y = \min(y_b, y_t)$, $n_z = \min(z_b, z_t)$ and (2) maximum values, $m_x = \max(x_b, x_t)$, $m_y = \max(y_b, y_t)$, $m_z = \max(z_b, z_t)$.

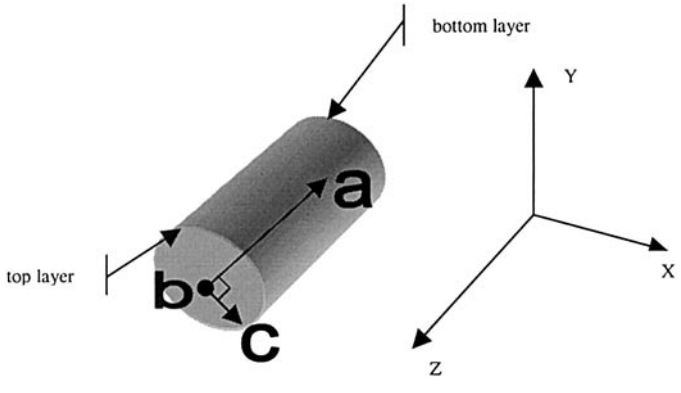

FIG. 10. Bottom and top layers of the cylinder.

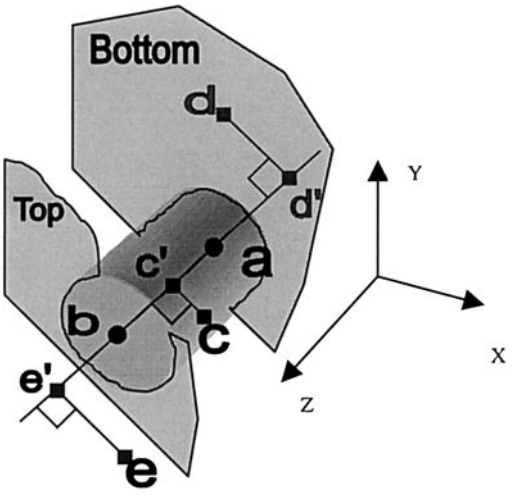

FIG. 11. Illustration of Condition 1: any point (x, y, z) belonging to the cylinder must be located between two planes containing the top and the bottom layers of the cylinder. Points d, e do not satisfy Condition 1 as they are not between planes Top and Bottom. Point c satisfies Condition 1 as it is between planes Top and Bottom.

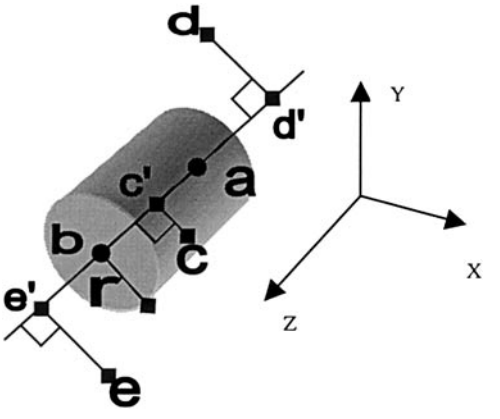

FIG. 12. Illustration of Condition 2: the distance between any point (x, y, z) belonging to the cylinder and the line going through segment ab should be less than or equal to the radius of cylinder r. Points d, e do not satisfy Condition 2 as the lengths of segments dd', ee' are bigger than the radius of cylinder r. Point c' satisfies Condition 2 as the length of segment cc' is smaller than the radius of cylinder r.

APPENDIX 2

Finding the Limits of the Third Coordinate for the Given Two Others

Assume that x and y are fixed. We are looking for the limit of z coordinate $[z_{min}, z_{max}]$ such that the whole segment ef, where $e = (x, y, z_{min})$ and $f = (x, y, z_{max})$, is inside the cylinder.

Any point x', y', z' lying on the axis of the cylinder (see segment ab in Fig. 6) has the following relationships with the superior and inferior tips.

$$\begin{cases} x' = x_1 + t(x_2 - x_1) \\ y' = y_1 + t(y_2 - y_1), \ 0 \le t \le 1. \\ z' = z_1 + t(z_2 - z_1) \end{cases} \tag{11}$$

For any point x, y, z lying in the plane perpendicular to axis ab, the scalar product of vectors $(x - x', y - y', z - z')$ and ab must be 0. Hence $(x_2 - x_1)(x - x') + (y_2 - y_1)(y - y') + (z_2 - z_1)(z - z') = 0$.

By using Eq. 11 to replace x', y', z', we get the equation for t

$$t = \frac{(x - x_1)(x_2 - x_1) + (y - y_1)(y_2 - y_1) + (z_2 - z_1)}{(x_2 - x_1)^2 + (y_2 - y_1)^2 + (z_2 - z_1)^2}$$
$$= \frac{(x - x_1)(x_2 - x_1) + (y - y_1)(y_2 - y_1) + (z - z_1)(z_2 - z_1)}{h^2}. \tag{12}$$

Since $0 \le t \le 1$, point x, y, z must satisfy (Fig. 11) Condition 1

$$0 \le \frac{(x - x_1)(x_2 - x_1) + (y - y_1)(y_2 - y_1) + (z - z_1)(z_2 - z_1)}{h^2} \le 1.$$

The distance from x, y, z to x', y', z' must be less than or equal to r. Thus, we get the next condition for x, y, z (Fig. 12), Condition 2

$$(x - x_1 - t(x_2 - x_1))^2 + (y - y_1 - t(y_2 - y_1))^2 + (z - z_1 - t(z_2 - z_1))^2 \le r^2.$$

Figure 13 illustrates a principle of determining the range of z for the fixed x and y. First, plane P is set such that it is parallel to plane XZ and passes through the fixed point $(x, y, 0)$. Next, the following calculations are done on plane P: 1. From Condition 1, we get the z range $[z_1, z_4]$. 2. From Condition 2, we get the z range $[z_2, z_3]$. 3. The calculated limit is $[z_{min}, z_{max}]$, where z_{min} is the maximum of z_1 and z_2, and z_{max} is the minimum of z_3 and z_4. So finally, the range is $[z_2, z_3]$.

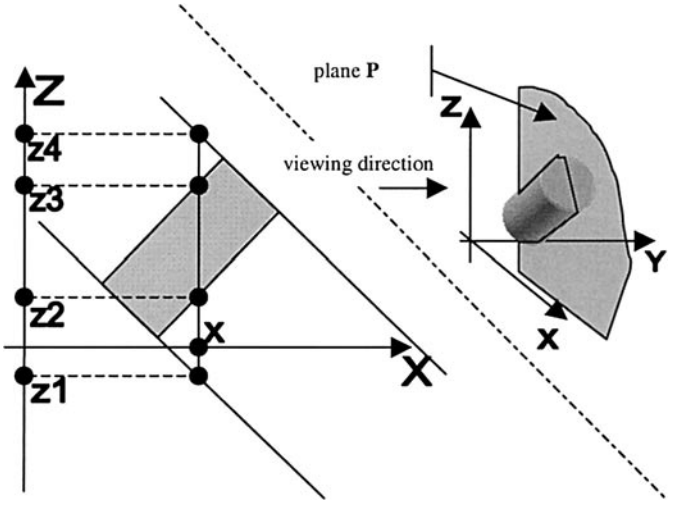

FIG. 13. Illustration of the principle for finding the z range.

From Condition 1, we get the condition for z as

$$\frac{-(x-x_1)k_1-(y-y_1)k_2}{k_3} \le z - z_1 \le \frac{h^2-(x-x_1)k_1-(y-y_1)k_2}{k_3},$$

where $k_1 = x_2 - x_1$, $k_2 = y_2 - y_1$, $k_3 = z_2 - z_1$. That gives the range of z as Condition 3

$$z_1 + D \le z \le z_1 + \frac{h^2}{k_3} + D,$$

where

$$D = \frac{-(x-x_1)k_1-(y-y_1)k_2}{k_3}.$$

Replacing t in Condition 2 by using Eq. 12 we get

$$((x-x_1)(h^2-k_1^2) - k_1k_2(y-y_1) - k_1k_3(z-z_1))^2 + ((y-y_1)(h^2-k_2^2) - k_1k_2(x-x_1) - k_2k_3(z-z_1))^2 + ((z-z_1)(h^2-k_3^2) - k_1k_3(x-x_1) - k_2k_3(y-y_1))^2 \le r^2h^4,$$

Denote by

$$A = (x-x_1)(h^2-k_1^2) - k_1k_2(y-y_1),\ a = k_1k_3,$$
$$B = (y-y_1)(h^2-k_2^2) - k_1k_2(x-x_1),\ b = k_2k_3,$$
$$C = -k_1k_3(x-x_1) - k_2k_3(y-y_1),\ c = (k_3^2 - h^2).$$

Then, the considered inequality can be rewritten as

$$(A - a(z-z_1))^2 + (B - b(z-z_1))^2 + (C - c(z-z_1))^2 \le r^2h^4$$
$$(a^2+b^2+c^2)(z-z_1)^2 - 2(aA+bB+cC)(z-z_1) + A^2 + B^2 + C^2 \le r^2h^4$$
$$(z-z_1)^2 - 2\frac{aA+bB+cC}{a^2+b^2+c^2}(z-z_1) \le \frac{r^2h^4-(A^2+B^2+C^2)}{a^2+b^2+c^2}$$
$$\left(z - z_1 - \frac{aA+bB+cC}{a^2+b^2+c^2}\right)^2 \le \frac{r^2h^4-(A^2+B^2+C^2)}{a^2+b^2+c^2} + \left(\frac{aA+bB+cC}{a^2+b^2+c^2}\right)^2.$$

Let

$$H = \frac{aA+bB+cC}{a^2+b^2+c^2} \text{ and } L = \frac{r^2h^4-(A^2+B^2+C^2)}{a^2+b^2+c^2} + H^2.$$

Hence, we get the condition for z as Condition 4

$$z_1 + H - \sqrt{L} \le z \le z_1 + H + \sqrt{L}.$$

By combining Conditions 3 and 4, we get the range of z, Condition 5,

$$n_z^{(x,y)} \le z \le m_z^{(x,y)},$$

where

$$n_z^{(x,y)} = \max(z_1 + H - \sqrt{L},\ z_1 + D)$$
$$m_z^{(x,y)} = \min\left(z_1 + H + \sqrt{L},\ z_1 + \frac{h^2}{k_3} + D\right).$$

For z to be in its range, $L \ge 0$. If $L < 0$, both x and y must have the extreme values such that there is no corresponding z within the cylinder.

We also consider special cases. In Case 1, $k_3 = 0$. Then

$$a = 0,\ b = 0,\ c = -h^2,\ C = 0,\ H = 0,\ L = \frac{(r^2h^4-(A^2+B^2))}{c^2}.$$

Taking into account Condition 1, we have $D = (x - x_1)k_1 + (y - y_1)k_2$. If $0 \le D \le h^2$ and $L \ge 0$, then $z_1 - \sqrt{L} \le z \le z_1 + L$. In Case 2, $k_1 = 0$ and $k_2 = 0$. Then $A = (x - x_1)h^2$, $a = 0$, $B = (y - y_1)h^2$, $b = 0$, $C = 0$, $c = 0$, $L = r^2h^4 - (A^2 + B^2)$. The sign of L has to be checked (as $(x - x_1)^2 + (y - y_1)^2 \le r^2$) and if $L = r^2 - (x - x_1)^2 + (y - y_1)^2 \ge 0$, then $z_1 \le z \le z_2$.

REFERENCES

1. Afshar, E., Watkins, E. S., and Yap, J. C. 1978. *Stereotactic Atlas of the Human Brainstem and Cerebellar Nuclei*. Raven Press, New York.
2. Andres, E., and Jacob, M. A. 1997. The discrete analytical hyperspheres. *IEEE Trans. Vis. Comp. Graphics* **3**(1): 75–86.
3. Andrew, J., and Watkins, E. S. 1969. A Stereotaxic Atlas of the Human Thalamus and Adjacent Structures. A Variability Study. Williams & Wilkins, Baltimore.
4. Benabid, A. L., Lavallee, S., Hoffmann, D., Cinquin, P., Le Bas, J. F., and Demongeot, J. 1992. Computer support for the Talairach system. In *Computers in Stereotactic Neurosurgery* (P. J. Kelly, and B. A. Kall, Eds.), pp. 230–245. Blackwell, Boston.

5. Chiavaras, M. M., LeGoualher, G., Evans, A., and Petrides, M. 2001. Three-dimensional probabilistic atlas of the human orbitofrontal sulci in standardized stereotaxic space. *Neuroimage* **13**(3): 479–496.
6. Cohen-Or, D., and Kaufman, A. 1995. Fundamentals of surface voxelization. *Graphical Models Image Process.* **57**(6): 453–461.
7. Grachev, D., Berdichevsky, D., Rauch, S. L., Heckers, S., Kennedy, D. N., Caviness, V. S., and Alpert, N. M. 1999. A method for assessing the accuracy of intersubject registration of the human brain using anatomic landmarks. *Neuroimage* **9**(2): 250–268.
8. Evans, A. C., Collins, D. L., and Milner, B. 1992. *An MRI-Based Stereotactic Brain Atlas from 300 Young Normal Subjects.* Proceedings of the 22nd Symposium of the Society for Neuroscience, Anaheim, 408.
9. Favre, J., Taha, J., Nguyen, T. T., Gildenberg, P. L., and Burchiel, K. J. 1996. Pallidotomy: A survey of current practice in North America. *Neurosurgery* **39**(4): 883–892.
10. Finnis, K. W., Starreveld, Y. P., Parrent, A. G., and Peters, T. M. 2000. A 3-dimensional database of deep brain functional anatomy, and its application to image guided neurosurgery. *Proc. 3rd International Medical Image Computing and Computer Aided Intervention Conference MICCAI 2000, Pittsburgh, PA, Oct 11–14,* pp. 1–8.
11. Foley, J. D., and van Dam, A. 1994. Introduction to Computer Graphics. Addison-Wesley, New York.
12. Fox, P. T., Mikiten, S., Davis, G., and Lancaster, J. L. 1994. BrainMap: A database of human functional brain mapping. In *Functional Neuroimaging: Technical Foundations* (R. W. Thatcher, M. Hallett, T. Zeffiro, E. R. John, and M. Huerta, Eds.), pp. 95–106. Academic Press, San Diego.
13. Gass, S. I. 1994. Linear Programming: Methods and Applications. McGraw–Hill, New York.
14. Hardy, T. L., Deming, L. R., and Harris-Collazo, R. 1999. Computerized stereotactic atlases. In Advanced Neurosurgical Navigation (E. Alexander III and R. J. Maciunas, Eds.), pp. 115–124. Thieme, Stuttgart.
15. Kall, B. A. 1992. Computer-assisted stereotactic functional neurosurgery. In *Computers in Stereotactic Neurosurgery* (P. J. Kelly and B. A. Kall, Eds.), pp. 134–142. Blackwell, Boston.
16. Kazarnovskaya, M. I., Borodkin, S. M., Shabalov, V. A., Krivosheina, V. Y., and Golanov, A. V. 1991. 3-D computer model of subcortical structures of human brain. *Comput. Biol. Med.* **21**(6): 451–457.
17. Le Goualher, G., Procyk, E., Collins, D. L., Venugopal, R., Barillot, C., and Evans, A. C. 1999. Automated extraction and variability analysis of sulcal neuroanatomy. *IEEE Trans. Med. Imaging* **18**(3): 206–217.
18. Lindgren, B. W. 1976. Statistical Theory. Macmillan, New York.
19. Mazziotta, J. C., Toga, A. W., Evans, A. C., *et al.* 1995. A probabilistic atlas of the human brain: Theory and rationale for its development. *NeuroImage* **2:** 89–101.
20. Mazziotta, J. C. 2000. Imaging: Window on the brain. *Arch. Neurol.* **57**(10): 1413–1421.
21. Miller, M., Banerjee, A., Christensen, G., Joshi, S., Khaneja, N., Grenander, U., and Matejic, L. 1997. Statistical methods in computational anatomy. *Stat. Methods Med. Res.* **6**(3): 267–299.
22. Niemann, K., van den Boom, R., Haeselbarth, K., and Afshar, F. 1999. A brainstem stereotactic atlas in a three-dimensional magnetic resonance imaging navigation system: First experiences with atlas-to-patient registration. *J. Neurosurg.* **90**(5): 891–901.
23. Niemann, K., and van Nieuwenhofen, I. 1999. One atlas–three anatomies: Relationships of the Schaltenbrand and Wahren microscopic data. *Acta Neurochir.* **141**(10): 1025–1038.
24. Nowinski, W. L. 1998. Anatomical targeting in functional neurosurgery by the simultaneous use of multiple Schaltenbrand-Wahren brain atlas microseries. *Stereotact. Funct. Neurosurg.* **71:** 103–116.
25. Nowinski, W. L., and Benabid, A. L. 2002. New directions in atlas-assisted stereotactic functional neurosurgery. In *Advanced Techniques in Image-Guided Brain and Spine Surgery* (I. M. Germano, Ed.), pp. 162–174. Thieme, New York.
26. Nowinski, W. L., Bryan, R. N., and Raghavan, R. 1997. The Electronic Clinical Brain Atlas. Multiplanar Navigation of the Human Brain. Thieme, New York.
27. Nowinski, W. L., Fang, A., Nguyen, B. T., Raphel, J. K., Jagannathan, L., Raghavan, R., Bryan, R. N., and Miller, G. 1997. Multiple brain atlas database and atlas-based neuroimaging system. *Comput. Aided Surg.* **2**(1): 42–66.
28. Nowinski, W. L. 2001. Modified Talairach landmarks. *Acta Neurochir.* **143**(10): 1045–1057.
29. Nowinski, W. L., Thirunavuukarasuu, A., and Kennedy, D. N. 2000. Brain Atlas for Functional Imaging. Clinical and Research Applications. Thieme, New York.
30. Ono, M., Kubik, S., and Abernathey, C. D. 1990. Atlas of the Cerebral Sulci. Thieme, Stuttgart.
31. Paus, T., Tomaiuolo, F., Otaky, N., MacDonald, D., Petrides, M., Atlas, J., Morris, R., and Evans, A. C. 1996. Human cingulate and paracingulate sulci: Pattern, variability, asymmetry, and probabilistic map. *Cereb. Cortex* **6**(2): 207–214.
32. Penhune, V. B., Zatorre, R. J., MacDonald, J. D., and Evans, A. C. 1996. Interhemispheric anatomical differences in human primary auditory cortex: Probabilistic mapping and volume measurement from magnetic resonance scans. *Cereb. Cortex* **6**(5): 661–672.
33. Schalkoff, R. J. 1992. Pattern Recognition: Statistical, Structural and Neural Approaches. Wiley, New York.
34. Schaltenbrand, G., and Bailey, W. 1959. Introduction to Stereotaxis with an Atlas of the Human Brain. Thieme, Stuttgart.
35. Schaltenbrand, G., and Wahren, W. 1977. Atlas for Stereotaxy of the Human Brain. Thieme, Stuttgart.
36. Sramek, M., and Kaufman, A. E. 1999. Alias-free voxelization of geometric objects. *IEEE Trans. Visualization Comp. Graphics* **5**(1): 251–267.
37. Sramka, M., Ruzicky, E., and Novotny, M. 1997. Computerized brain atlas in functional neurosurgery. *Stereotact. Funct. Neurosurg.* **69**(1–4 Pt. 2): 93–98.
38. Talairach, J., David, M., Tournoux, P., Corredor, H., and Kvasina, T. 1957. Atlas d'Anatomie Stereotaxique des Noyaux Gris Centraux. Masson, Paris.
39. Talairach, J., and Tournoux, P. 1988. Co-Planar Stereotactic Atlas of the Human Brain. Thieme, Stuttgart.
40. Talairach, J., and Tournoux, P. 1993. Referentially Oriented Cerebral MRI Anatomy. Atlas of Stereotaxic Anatomical Correlations for Gray and White Matter. Thieme, Stuttgart.
41. Tasker, R. R., Hawrylyshyn, P., and Organ, W. 1978. Computerized graphic display of physiological data collected during human stereotactic surgery. *Appl. Neurophysiol.* **41:** 187–193.
42. Thompson, P. M., MacDonald, D., Mega, M. S., Holmes, C. J., Evans, A. C., and Toga, A. W. 1997. Detection and mapping of abnormal brain structure with a probabilistic atlas of cortical surfaces. *J. Comput. Assist. Tomogr.* **21**(4): 567–581.
43. Thompson, P. M., Woods, R. P., Mega, M. S., *et al.* 2000. Mathematical/computational challenges in creating deformable and

probabilistic atlases of the human brain. *Hum. Brain Mapp.* **9**(2): 81–92.

44. Toga, A. W. (Ed.) 1998. Brain Warping. Academic Press, San Diego.
45. Toga, A. W., and Thompson, P. M. 2001. Maps of the brain. *Anat. Rec.* **265**(2): 37–53.
46. Van Buren, J. M., and Borke, R. C. 1972. Variations and Connections of the Human Thalamus. Springer-Verlag, New York.
47. Van Essen, D. C., Lewis, J. W., Drury, H. A., Hadjikhani, N., Tootell, R. B., Bakircioglu, M., and Miller, M. I. 2001. Mapping visual cortex in monkeys and humans using surface-based atlases. *Vision Res.* **41**(10–11): 1359–1378.
48. Yoshida, M. 1992. Three-dimensional maps by interpolation from the Schaltenbrand and Bailey atlas. In *Computers in Stereotactic Neurosurgery* (P. J. Kelly and B. A. Kall, Eds.), pp. 143–152. Blackwell, Boston.
49. Nowinski, W. L., Belov, D., and Benabid, A. L. A community-centric Internet portal for stereotactic and functional neurosurgery with a probabilistic functional atlas. *Stereotact. Funct. Neurosurg.*, in press.